Interaction of Saturn's magnetosphere and its moons: 2. Shape of the Enceladus plume

Y.-D. Jia,[1] C. T. Russell,[1,2] K. K. Khurana,[1] Y. J. Ma,[1] D. Najib,[3] and T. I. Gombosi[3]

[1] The Saturnian moons in the inner magnetosphere are immersed in a plasma disk that rotates much faster than the moon's Keplerian speed. The interaction of the rotating plasma with the moons results in a disturbance in the Saturnian magnetospheric plasma that depends on the nature of obstacle that the moon represents. In particular at Enceladus, such perturbations in the magnetic field and flowing plasma enable us to infer the 3-D shape of the Enceladus plume and its outgassing rate. In this paper, we apply our 3-D magnetohydrodynamic model to extensively study the effects of different plume and disk plasma conditions on the interaction. By finding the best agreement with the observations of two diagnostic flybys, one with its point of closest approach on the upstream side and the other on the downstream side, we determine the plume intensity and configuration. We find that mass loading in the plume is less efficient close to the surface of the moon, where the neutral density is the highest. For E2 and E5, the opening angle of the plume is about 20°, and the plume is tilted toward the corotating direction. The upstream density has a significant effect on the mass loading rate, while its effect on the magnitude of the magnetic perturbation is less significant. An upstream velocity component in the Saturn direction helps to explain the observed magnetic perturbation in the B_y component and signals the need to consider Enceladus's effect on the global plasma circulation in addition to the local effect. Quantitative comparisons of the simulated and observed interaction are provided.

1. Introduction

[2] The major gas-producing moon in the Saturnian system, Enceladus, is located at 3.95 Saturn radii, where the magnetic field is strong and the plasma is relatively cold. The signature of gas production and the resulting mass loading of the corotating plasma are directly revealed in the magnetic field perturbations that arise when the fast-rotating plasma interacts with Enceladus and its plume [*Dougherty et al.*, 2006]. Recent Cassini observations have been obtained on seven Enceladus flybys with their points of closest approach on both the upstream and the downstream sides. These observations have revealed an extensive, asymmetric water plume emanating from the south polar region of this icy moon [*Waite et al.*, 2006; *Hansen et al.*, 2006]. The magnetic field data collected from these flybys have clarified the importance of Enceladus gas production for the maintenance of the E ring surrounding Saturn. In addition, these observations allow us to determine the spatial distribution of the neutral cloud and its temporal variation.

[3] The interaction of the plasma flow with Enceladus is complex. The flow interacts with the surface of the moon, with an exosphere, and with the plume gas and dust. In this series of studies, we use our 3-D magnetohydrodynamic (MHD) code to model the interaction. In paper 1 [*Jia et al.*, 2010a], we examined the basic interaction processes: the interaction with pure absorbing nonconducting body and an interaction with an exosphere that supplies ions via different types of ionization processes. This paper (paper 2) uses the model introduced in paper 1 to investigate the interaction with the Enceladus plume using a self-consistent MHD model that enables detailed quantitative comparisons with the 2008 flybys. This model was not available to assist with previous studies [e.g., *Tokar et al.*, 2006; *Burger et al.*, 2007; *Khurana et al.*, 2007; *Saur et al.*, 2008, and references therein]. Herein we determine the configuration of the mass loading plume and its effect on the flow. In paper 3, we determine the spatial and time variation of the Enceladus plume using all seven Cassini flybys in 2005 and 2008 (Y.-D. Jia et al., Interaction of Saturn's magnetosphere and its moons: 3. Time variation of the Enceladus plume, manuscript in preparation, 2010).

[4] Model-data comparisons are presented in this paper using two typical flybys, E2 and E5 flyby. The E2 flyby has

[1]IGPP, University of California, Los Angeles, California, USA.
[2]Department of Earth and Space Science, University of California, Los Angeles, California, USA.
[3]Department of Atmospheric, Oceanic and Space Sciences, University of Michigan, Ann Arbor, Michigan, USA.

a closest approach on the upstream side, while E5 has its closest approach on the wake side. During the E2 flyby on 14 July 2005, Cassini went primarily from south to north of Enceladus, while the magnetometer has seen magnetic perturbations in all three components. It is suggested that the mass loading center is at 3.5 R_E south and 2.5 R_E downstream of Enceladus [*Khurana et al.*, 2007]. The E5 flyby is primarily a north-south flyby on 9 October 2008, which is determined to study the Enceladus plume after its discovery in 2005. In addition, during the E5 flyby, Cassini passed close to the center of the plume with the closest approach 27 km from the surface. The Cassini magnetometer has found large perturbations to the magnetic field components, extending from 5 R_E above Enceladus to 10 R_E below Enceladus, as shown by the black solid lines in Figure 3.

[5] In this paper we simulate the steady state interaction between the torus flow, Enceladus and its plume, to reproduce the 3-D plasma environment around Enceladus, by comparing our model result with the magnetometer data. The simulation model, the physical parameters of the interacting plasma and the background water plume are described in section 2. The detailed physical conditions, including the gas production rate, the plume opening angle, plume tilt angle, and the upstream conditions are presented in section 3. Section 3.7 also quantifies the mass loading contribution of the charge-exchange and photo/impact-ionization processes. Section 4 summarizes and concludes this paper.

2. Model Description

[6] The interaction between the planetary torus plasma and a gas-producing moon is characterized by a complex system involving the sub-Alfvenic torus plasma flow, the corotating planetary magnetic field, the newly picked-up plasma around the moon, the ejected neutral particles, and the moon's surface. The model used is the Cassini magnetometer data (with constraints from other instruments) and the (Block Adaptive Tree Solar-wind Roe Upwind Scheme) BATS-R-US, a 3-D global MHD model developed and managed at the University of Michigan [*Powell et al.*, 1999; *Tóth et al.*, 2005]. The governing equations are the mass-loaded ideal MHD equations described in paper 1 [*Jia et al.*, 2010a].

2.1. Neutral Atmosphere

[7] To simulate the mass loading effect of the Enceladus neutral atmosphere, multiple neutral distributions are tested. The Enceladus atmosphere is represented by a spherically symmetric component plus a plume component originating from the south pole and directing to the south. The density of both components, n_{ns} and n_{np}, decreases with the distance from its origin. This distance dependency neglects modification of the neutral densities by the gravity force, photon-neutral processes or collision with the plasmas. There are charged dust particles ejected with the neutral particles that may interact with the corotating plasma [*Jones et al.*, 2009; *Farrell et al.*, 2009]. These particles may cause some localized perturbations to the magnetic field (primarily in B_x and B_y) but are neglected in our current simulations that focuses on the overall intensity of the mass loading and the general shape of the plume. Further studies with the charged

dust components are needed to address the physics at the plume center more accurately.

[8] The neutral density in the spherically symmetric component is described as:

$$n_{ns} = \frac{Q_s}{4\pi u_n r^2} \tag{1}$$

where $r = \sqrt{x^2 + y^2 + z^2}$ is the radial distance, and $Q_s = 8 \times 10^{25}$ s^{-1} is the gas production rate by surface sputtering [*Burger et al.*, 2007]. The neutral velocity, $u_n = 0.3$ km/s is assumed to be constant [*Hansen et al.*, 2006]. In paper 1, it is found that in a range of 0 to 5 km/s, the effect of this u_n is not observable from our magnetic field results. For the paper 1 cases, the flow is not significantly decelerated, so the flow speed is one to two orders of magnitude larger than the neutral speed in this frame. For the paper 2 cases, the plume ejection is primarily aligned with the field so the result is not sensitive to the neutral speed.

[9] In the plume, n_{np} is adjusted by a plume opening angle θ_H. The density falls to r_p^{-2}, which is the distance to the origin of the plume. The plume component can be written as:

$$n_{np} = \frac{Q_p}{A u_n r_p^2} e^{\left(-(\theta/\theta_H)^2 \ln 2\right)}, \tag{2}$$

where $r_p = \sqrt{x^2 + y^2 + (z+1)^2}$ in units of R_E is the distance to the south pole, Q_p is the gas production rate assumed to be constant during the time scale of a flyby, θ is the location angle from the south pole relative to the plume axis, θ_H is the half width of the neutral jet flow. In addition, A is an integration constant depending on θ_H. The value of A is determined so that the total flux across any closed surface surrounding the Enceladus body equals Q_p. For $\theta_H = 10°$, $20°$, $25°$, $A \approx 0.13706$, 0.536, 0.82446, respectively [*Jia et al.*, 2008].

[10] As suggested by the magnetometer data, the plume density is modified into the form of n'_{np} to simulate the lack of charge exchange and impact ionization close to the south pole:

$$n'_{np} = n_{np} \times e^{\left(-\alpha\left(R_{p0}-r_p\right)\right)}, r_p < R_{p0}$$

$$n'_{np} = n_{np}, else \tag{3}$$

where R_{p_0} is the distance within which to apply the reduction, $R_{p_0} = 1.8$ R_E is used in this work. Parameter α is the scaling factor that is determined to be 2.8 from the best fit to both flybys.

[11] To simulate the possible tilt of the plume axis as suggested by the surface images [*Spitale and Porco*, 2007], a tilt angle θ_T is defined by rotating the plume coordinate system about its y axis. Rotations about the x axis are also studied but their effect on the field perturbations are less obvious compared with the y axis rotations so they are not presented here.

[12] The sum of the two components defined by equations (1) and (2) are used in our simulation model. As shown in Figure 1a, the neutral density of the plume component is over three orders of magnitude larger than that of the spherical component close to the plume center. It is also
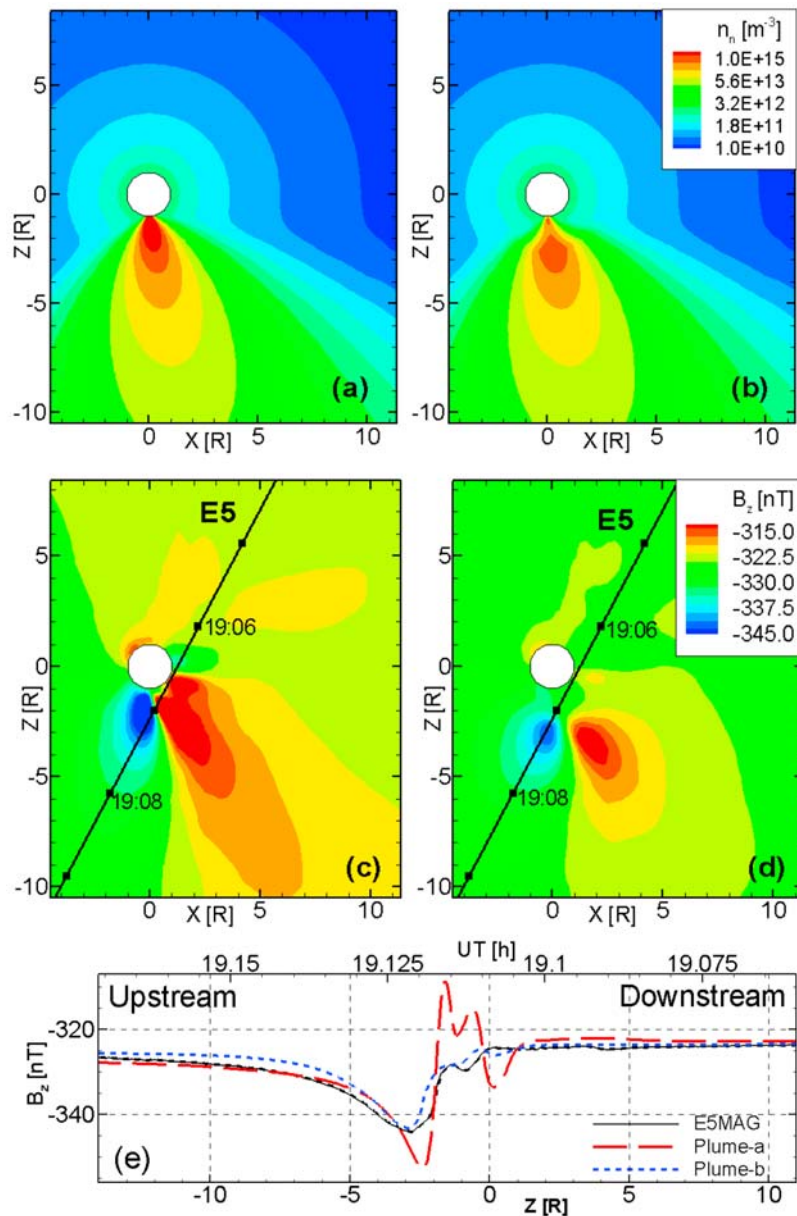
Figure 1. Slices at $y = 0$ showing the effect of mass loading close to the surface. Enceladus is represented by the white circle. (a) The neutral density defined by equation (2). (c) The result is shown as B_z contours. (b) The neutral density defined by equation (3). (d) The resulting B_z component and Cassini E5 trajectory are shown. (e) The values are compared with the line plot. Thin solid line is the Cassini observations. The red dashed line is the plume a result, while the dotted line is the plume b result.

found in paper 1 [*Jia et al.*, 2010a] that the measured B_y perturbation is over an order of magnitude stronger than that created by the spherically symmetric component. Thus at this stage, we use the data to determine the configuration of the plume component, while the intensity of the spherically symmetric component is not constrained by the observations.

[13] The ion pickup processes include photo/impact ionization and charge exchange. All ion species are grouped into one single water species with an average mass 17 amu. The two major electron-creating ionization processes are photoionization and electron impact ionization: $f_i = f_{ph} + f_{imp}$. Among these, the photoionization rate can be estimated from the 1 AU value for quiet sun conditions as $f_{ph} = 5 \times 10^{-9}$ s^{-1}. The electron impact ionization process is dependent on the population and temperature of the hot electrons [*Cravens et al.*, 1987; *Tokar et al.*, 2006], while in this work a constant of $f_{imp} = 1.5 \times 10^{-8}$ s^{-1} is adopted [*Burger et al.*, 2007]. The effect of variations in impact ionization, including the dependence of ionization rate on electron energy, is discussed in paper 3 (Jia et al., manuscript in preparation, 2010). The charge-exchange reactions between water group ions and neutrals are simplified into a single species reaction with reaction rate $k_{in} = 2 \times 10^{-15}$ m^3 s^{-1} [*Huntress*, 1977]. This rate assumes a reaction energy lower than 1 eV which
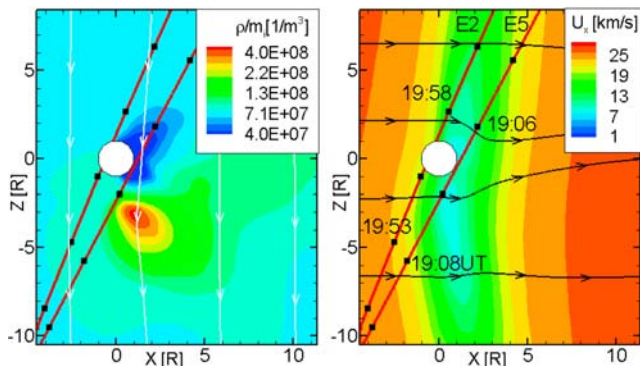
Figure 2. Plasma distributions in the $y = 0$ slices. E2 and E5 trajectories are projected as red lines with universal time marked in Figure 2 (right). Figure 2 (left) shows plasma number density; Figure 2 (right) shows the x component of flow velocity. White lines are field lines, while black lines are stream lines. From left to right, the coordinates of the five black squares on the E2 trajectory are $(-4.1, -5.0, -8.5)$; $(-2.6, -2.1, -4.9)$; $(-1.0, 0.9, -1.1)$; $(0.6, 3.9, 2.7)$; and $(2.2, 6.7, 6.3)$ R_E. Those for E5 are $(-3.76, 0.5, -9.5)$; $(-1.79, 0.2, -5.8)$; $(0.2, 0.0, -2.0)$; $(2.2, -0.3, 1.8)$; and $(4.2, -0.5, 5.6)$ R_E.

is accurate only close to the center of the mass loading region. The effect of an energy-dependent charge-exchange rate is discussed in paper 3 (Jia et al., manuscript in preparation, 2010).

2.2. Physical Conditions

[14] Enceladus is located in the inner magnetosphere of Saturn, where the corotating plasma flow is not affected by the solar wind. For both flybys, the torus plasma density, velocity, and temperature are set to be nominal values at the Enceladus orbit: $n_{i_0} = 70$ cm^{-3}, $u_0 = 26.4$ km/s, $T_0 = 4 \times 10^5$ K. The Saturnian magnetic field strength is approximately 330 nT. These conditions result in a plasma β value of 0.01, Alfvenic Mach number $M_A = 0.1$, and sonic Mach number $M_s = 1.5$. More details of the background characteristic speeds are described in Figure 2 of paper 1.

[15] As can be seen from Figure 1e, the background field is not uniform in the calculation domain. The primary reason is due to the geometry of the Cassini trajectories. The y axis is the Saturnian radial direction so any changes in y location of the spacecraft results in a change in the distance (r_s) to Saturn and thus a change in field strength proportional to r_s^3.

[16] In our model, the Saturnian dipole field is applied to the calculation domain to be compared with the observations. The field strength is 20800.0 nT on the Saturnian equator at the distance of one Saturn radius (Rs). The dipole center is 2.3802×10^5 km in the $+y$ direction from the origin at the center of Enceladus. The resulting value is less than 20 nT different from the observed value that includes the plasma perturbations to the field. Within the plotted domain, these differences are constant so they can be corrected by uniformly shifting the background (presented in section 3.3).

[17] The flow speed is 27 km/s, while the ion thermal speed is around 20 km/s. Thus the curvature-drift speed and

the gradient-drift speed of water group ions in such a dipole field are approximately 2 km/s, an order of magnitude smaller than the flow speed and thermal speed. This is consistent with the fact that the Saturnian ring current is beyond 8 Saturn radii [*Connerney et al.*, 1981], where the corotation speed is over two times larger and the plasma is hotter. In addition, a test case with a uniform magnetic field of 330 nT (not plotted here) is studied. No significant difference is seen in the modeled field perturbations. In future studies when the force balance and planetary rotation are considered, differences are expected and the dipole field will be more appropriate than a uniform background field.

[18] The Enceladus surface is represented as an absorbing body with a nonconducting surface. As found in paper 1, the magnetic perturbation along the trajectories past the body due to absorption is less than 10% of the observed value. To confirm our previous result we have compared (not shown) the B_z perturbation along the E5 trajectory. To study the effect of the inner boundary, two test cases are compared. One is the best fit case that is presented in section 3.3; the other has no Enceladus body while all other settings are kept the same as in the best fit case. The density distribution is significantly different between cases with or without the body. However, the difference in magnetic field perturbations is limited to the body wake region and the intensity difference is less than 10%. The reason for the behavior can be found in the geometry of the interaction region. The magnetic field is strong and perpendicular to the plasma flow. Thus the magnetic pressure is dominant in the wake region ($\beta = 0.01$ in the background). A small change in the field strength can balance the difference caused by the density gradient. Based on these tests we choose the same boundary conditions as in the nonconducting absorbing body case studied in paper 1.

[19] Unless specified otherwise, the gas production rate used for both E2 and E5 flyby conditions is 2.8×10^{28} s^{-1}. The typical values of these parameters are summarized in Table 1 of paper 1 [*Jia et al.*, 2010a].

[20] The grid system in our $80 \times 80 \times 80$ R_E domain is the same as used in paper 1, where R_E is the radius of Enceladus. The coordinate system is also the ENIS system, where X is along the direction of corotational flow and Y is positive toward Saturn [*Dougherty et al.*, 2006].

3. Model Results

[21] Among the seven flybys to Enceladus, E2 and E5 are both north-south flybys. The naming convention for the flybys is to use the first letter of the moon (in this case E for Enceladus) and append the sequential number of the encounter beginning with the more distant E0 encounter in which the Enceladus plume interaction was discovered [*Dougherty et al.*, 2006]. As projected in the $x - z$ plane in Figure 2, the closest approach of E2 is on the upstream side (so E2 is also called the "upstream flyby" in this paper), while that of E5 is on the wake side (E5 is named the "downstream flyby" for the same reason). Among the flybys before the end of year 2008, E2 is the closest upstream flyby [see *Khurana et al.*, 2007, Figure 2] while E5 has a similar trajectory to the other downstream flybys [*Tokar et al.*, 2009; *Jia et al.*, 2010b]. We focus all our case studies (as summarized in Table 1) on these two flybys to show

Table 1. Summary of Case Studies

Case	Q^a	$\theta_H°$	$\theta_T°$	$n_{i\infty}$ (cm^{-3})	$u_{y\infty}$ (km/s)	f_{in}^b	k_{in}^c	n_n
1	2.8	20	10	70	0	1	1	n_{np}
2	2.8	20	10	70	0	1	1	n'_{np}
3	2.0	20	10	70	0	1	1	n'_{np}
4-Tilt0	2.8	20	0	70	0	1	1	n'_{np}
4-Open10	2.8	10	10	70	0	1	1	n'_{np}
5-Uy15	2.8	20	10	70	15	1	1	n'_{np}
5-R4	2.8	20	10	40	0	1	1	n'_{np}
6-CX	2.8	20	10	70	0	0	1	n'_{np}
6-Ini	2.8	20	10	70	0	1	0	n'_{np}

[a]In units of [10^{28} s^{-1}].
[b]In units of [2×10^{-8} s^{-1}].
[c]In units of [2×10^{-15} m^3/s].

the effect of plasma and plume conditions on the interaction, so as to quantify these conditions from observations.

3.1. Case 1 and Case 2: Effectiveness of Mass Loading Close to the South Pole

[22] As shown in "case 3" of paper 1, a mass loading region results in an upstream increase followed by a downstream decrease of the absolute value of B_z. However, Cassini passed downstream of the Enceladus plume during its E5 flyby without seeing any decrease from the background $|B_z|$. Here in cases 1 and case 2, we simulate the interaction between the torus plasma and the plume source, with full and reduced mass loading close to the surface, respectively.

[23] The two types of neutral density profiles used in this study are plotted in Figures 1a and 1b. The colored contours are neutral density contours with the same set of levels. Figure 1a shows a plume defined by equation (2). The result of the first interaction is the case 1 result, as shown with magnetic B_z component contours in Figure 1c. Figure 1b shows a plume defined by equation (3). Its result, namely the case 2 result, is shown in Figure 1d. Other parameters used in these two cases are kept the same, as summarized in Table 1. Close to the south pole (in the red region), there are clear differences between the results of the two types of plumes. In addition, the region with a $|B_z|$ increase is closer to the body than observed.

[24] In Figures 1c and 1d, there is also an increase-decrease pair in the B_z component downstream of the point $(-1, 0, 0)$ R$_E$. This is due to the plasma flow along the $\pm z$ direction in the wake (see Figure 1e in paper 1). Because of the plasma deceleration at the plume center, a negative B_x component is created in this region. The u_z flow in the $-z$ direction above the $z = 0$ plane turns this B_x component into the $-z$ direction. Below the $z = 0$ plane, the flow in $+z$ direction tends to decrease the B_z component and increase the B_x component. Compared with "case 4" in paper 1, this is a new feature when the mass loading center has an offset along the field from the center of absorber. A test with the spherically symmetric mass loading center displaced to $(0, 0, -1)$ R$_E$ results in similar disturbance pattern in B_z, as shown in the subcase of their case 4 in paper 1.

[25] Figure 1e compares the results of case 1 and 2 and the magnetometer measurements of the B_z component along the Cassini trajectory. The case 1 result is shown as the red dashed lines, case 2 is the blue dotted lines, while the solid black line is the Cassini observation during its E5 trajectory.

Case 2 reproduces the B_z observation while case 1 dose not. There are significant decreases in $|B_z|$ between 0 and -2 R$_E$, which is not seen by Cassini. This comparison shows that decreasing the rate of ion-neutral interactions within 1.8 R$_E$ of the south pole, as defined by equation (3), can better reproduce the magnetometer observations.

[26] Our tests have shown that by changing other parameters, such as the tilt angle and opening angle of the plume, the large decreases in $|B_z|$ cannot be removed, suggesting that the mass loading rate in the part of plume between the south pole and $r = 2.8$ R$_E$ is not as strong as that of the plume outside this distance. This could be produced in several ways: the hot electrons that cause electron impact ionization may be depleted inside the neutral jets where neutral density is high [*Farrell et al.*, 2009]; the neutral density may be concentrated in thin jets closer than this distance, possibly subgrid scale, which cannot be accurately modeled by our single broad plume model; or the ejecta may not be fully vaporized. Our tests (not shown here) reveal that without this modification, the perturbation to the magnetic field is more sensitive to the parameters than shown in cases 3, 4 and 5. More detailed study is needed of this region, while more observations probing the downstream side of the plume (preferably below 2.8 R$_E$) are expected to see the decrease of $|B_z|$.

3.2. Reconstruction of the Interaction Environment

[27] Using comparisons discussed in section 3.1, the neutral plume configuration, described in equation (3), is selected for all following comparisons to determine the best set of parameters for the configuration of the plume. Shown in Figure 2 are steady state $y = 0$ slices of the interaction environment during the E5 flyby conditions reproduced by our best fit (case 2 result). E2 and E5 trajectories are projected into this $y = 0$ plane, with universal time marked in the format of hour:minutes.

[28] In the density contours shown in Figure 2 (left), a wake of decreased density is formed behind Enceladus. The pickup process from the plume neutrals forms a region with a maximum density about five times greater than that of the upstream flow. The location of this density peak is at $(1, 0, -3.2)$ in units of R$_E$, making it the center of the mass loading region. The white field lines show slight bending by ion pickup.

[29] In Figure 2 (right), the x component of velocity decreases from 26.4 km/s to approximately 8 km/s in the plume center, to create a pair of Alfven wings. The Alfven wings are displaced approximately 2.5 R$_E$ southward, because of the displacement of the mass loading center. Compared with the "case 4" result of paper 1 where the flow is aligned in the x direction, the north and south wings start at different z values at different x locations due to the northward flow that fills the wake. With this significant u_z, the flow is no longer dominated by u_x. The angle of the northern wing is further modified by the nonconducting body and its wake flow. Well downstream, the angle of the Alfven wings are both 83°, while the angular change in the northern wing across the body and its wake are less than 5°.

[30] The black stream lines show expansion downstream of the body into the wake, and expansion from the region with the maximum pickup. The boundary of the expansion
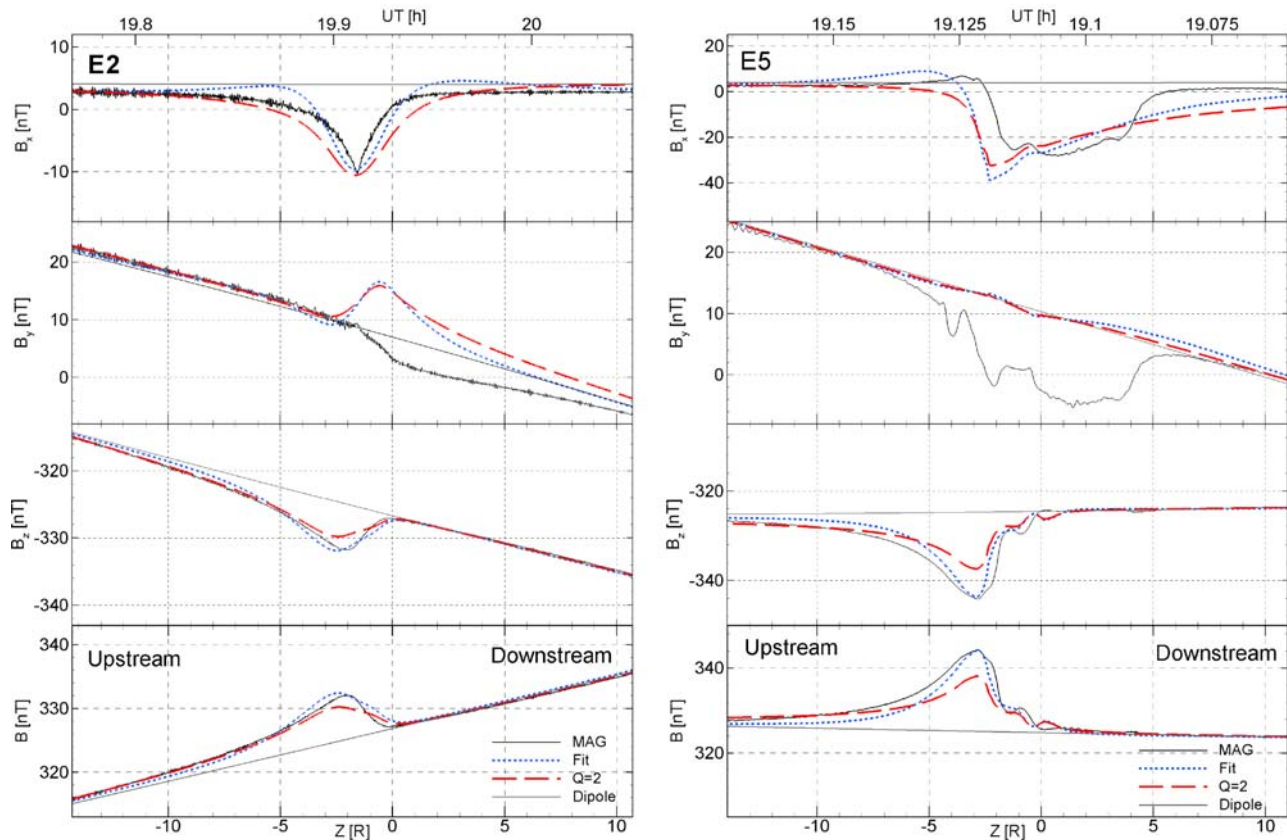
Figure 3. Magnetic field components along the Cassini trajectories from our model result compared with the (left) E2 and (right) E5 flybys. The solid black lines represent the Cassini data (marked "MAG"), the best fit result is represented by the blue dotted lines (marked "Fit," as in Figures 4–6), and the dashed lines show a simulation result with 30% less gas production rate (marked "Q = 2"). The grey straight lines (marked "Dipole" in the legend) are the background value that we used in our model. Both E2 and E5 are plotted against the z axis, from upstream to downstream. Please note the difference in time sequences.

fan is around 40° from the x axis and is not as smooth as the 35° expansion fan in "case 1" and "case 4" of paper 1, due to the flow from the mass loading center. The region with z deflection of the flow is limited between $z = -5$ and $z = +5$ R_E, while the y extension (not shown) of this deflection is also smaller than 5 R_E. The size of the region of flow perturbation is an order of magnitude smaller than the value [*Tokar et al.*, 2006; *Pontius and Hill*, 2006] calculated using Cassini plasma data. We interpret the Saturnward flow that [*Tokar et al.*, 2006] observed as a hint of the existence of a large-scale flow pattern, instead of a flow disturbance caused by local interactions that we model here. Further analysis of such a flow is presented in section 3.6.

3.3. Case 2: Best Fit for E2 and E5

[31] In this section we reexamine the case 2 result using the three components and magnitude of the magnetic field. As summarized in Table 1, the gas production rates used for the E2 and E5 flybys are both 2.8×10^{28} s^{-1}. The resulting mass loading rate for both flybys is 0.94 kg/s. The plume tilts 10° to downstream, while the opening angle is 20°. The reason why we choose these parameters are discussed in following sections. The criteria used to determine the best fit is based on the B_z difference between $z = 0$ and $z = -5$ R_E for E2 cases and $z = 0$ and $z = -10$ R_E for E5. The difference is

calculated by $\sqrt{\sum (B_{z,model} - B_{z,mag})^2}$, where subscripts "model" and "mag" represent the model results and the observations, respectively.

[32] Figure 3 shows case 2 result compared with the Cassini measurement in all three components and the magnitude of magnetic field. Figure 3 (left) shows the values along the E2 trajectory, while Figure 3 (right) shows the values along E5. The thin solid lines are the observations, which are marked "MAG." The grey straight lines (marked "Dipole") show the background value that is applied to our model. The dotted lines show the best fit case, which are marked "Fit" in the legends, respectively. The dashed lines are discussed in section 3.4.

[33] Compared with the observations, the B_z components are well reproduced in both cases. However, the B_y perturbation created by the plume is different from the observation. We interpret this as the effect of a radial component of the convective flow (in the y direction). The effect of such flows is further discussed in section 3.1 using case 5.

[34] Consequently, the B_x fit is not as effective as the B_z fit. In addition, the mass loading rate is used to determine the plume intensity. Because the magnetic field is primarily in the z direction, and the trajectory is mainly along z, the mass loading rates can be probed by examining the maximum perturbation to B_z, or B. Since in this study we are
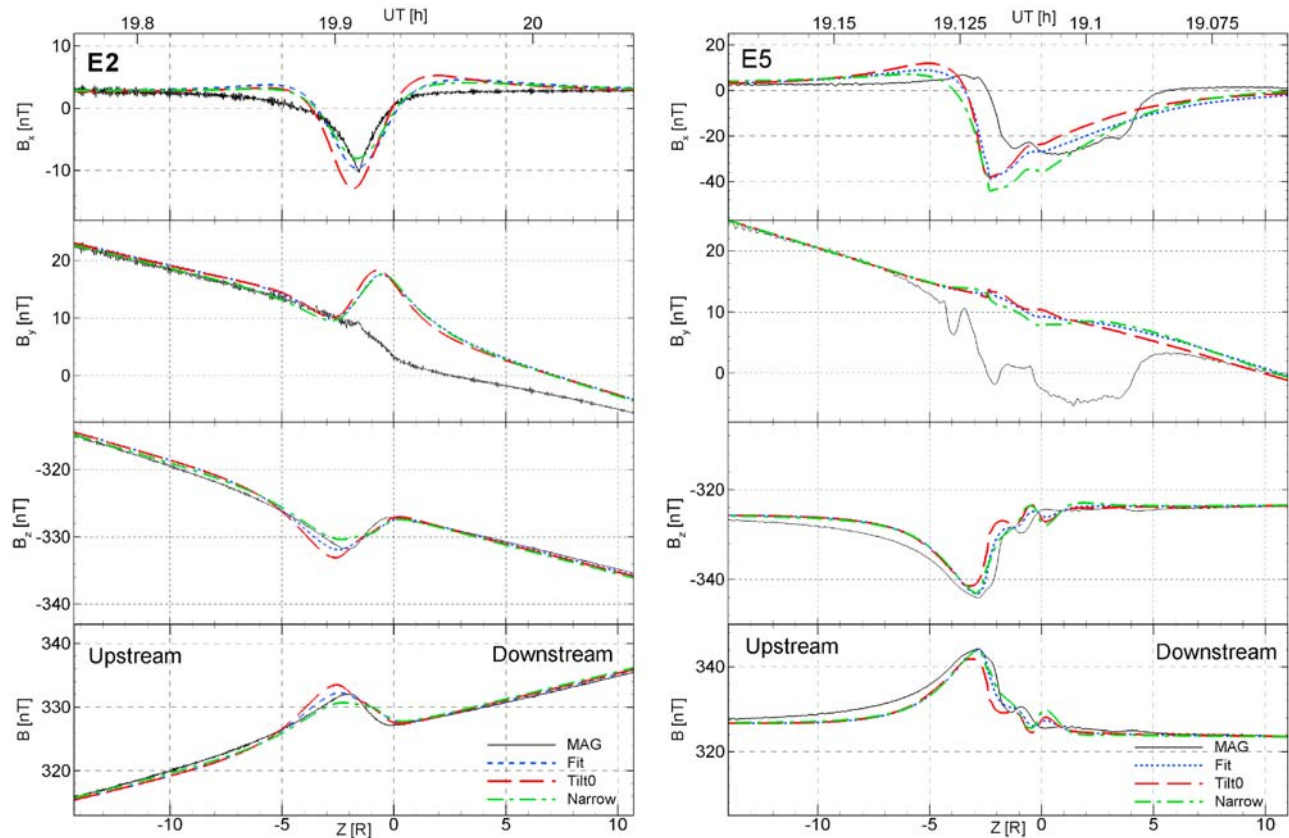
Figure 4. Model-data comparison for the magnetic field components along the Cassini trajectories. With (left) E2 and (right) E5, different model lines show the effects of different plumes. The blue dotted lines show the best fit model results, the dashed lines show the model result with a plume along the $-z$ axis (0 tilt angle), and the green dash-dotted lines show the results with a narrower and tilted plume (10° opening angle).

using trajectories optimized for studying the plume intensity and not the radial flow, we attempt only to optimize the fit to B and B_z. The maximum density along the E2 trajectory is consistent with the INMS observation shown by *Waite et al.* [2006].

[35] Previous observations estimate the gas production rate at Enceladus as 10^{28} s^{-1}, which is smaller than the value used in our model. In addition, *Burger et al.* [2007] and *Saur et al.* [2008] estimated a gas production rate of 10^{28} s^{-1} during the E2 flyby as well. On the other hand, the mass loading rate that *Khurana et al.* [2007] and *Saur et al.* [2008] estimated from the E2 flyby is consistent with our estimate. This is because our charge-exchange rate that is optimized for low relative-interaction velocity is smaller than that used by *Burger et al.* [2007]. A multispecies MHD model that calculates the water group charge-exchange reactions with a velocity-dependent function should be used to determine the total gas production rate more accurately from the magnetometer data.

3.4. Case 3: Effect of Different Production Rates

[36] The red dashed lines in Figure 3 represent the case 3 result with a lower gas production rate of $Q = 2.0 \times 10^{28}$ s^{-1}. Thus the gas production rate is 29% less than that is used in all other cases. Consequently, The maximum B perturbation caused by this case 3 is 37% (E2) and 31% (E5) smaller than

that of the case 2 results. In addition, the mass loading rate in this case 3 is 16% less than that in case 2. The difference between the mass loading ratio and the indicated gas production ratio is due to the ineffectiveness of mass loading in the regions close to the south pole, as discussed in section 3.1.

[37] By comparing the effect of gas production rate for E2 and E5 flybys we can see that the perturbation to the magnetic field is sensitive to the gas production rate. Consequently, gas production rates can be inferred by achieving the model fit with the magnetometer data of these flybys.

3.5. Case 4: Configuration of the Plume

[38] In this section we present our case 4 results with two subcases compared to the observation and our best fit. To better understand the shape of the plume, the effects of different plume configurations are shown as different lines in Figure 4. The thin solid lines are the magnetometer data, the dotted lines are the case 2 results, the dashed lines are the results with the same opening angle but 0° tilt angle (named case "4-Tilt0" in Table 1 and "Tilt0" in the legend). The dash-dotted lines are the results with a 10° tilt and 10° opening angle (named case "4-Open10" in Table 1 and "Narrow" in the legend).

[39] Compared with the observations, for the E2 flyby, a 0° tilt angle results in displaced maximum locations with
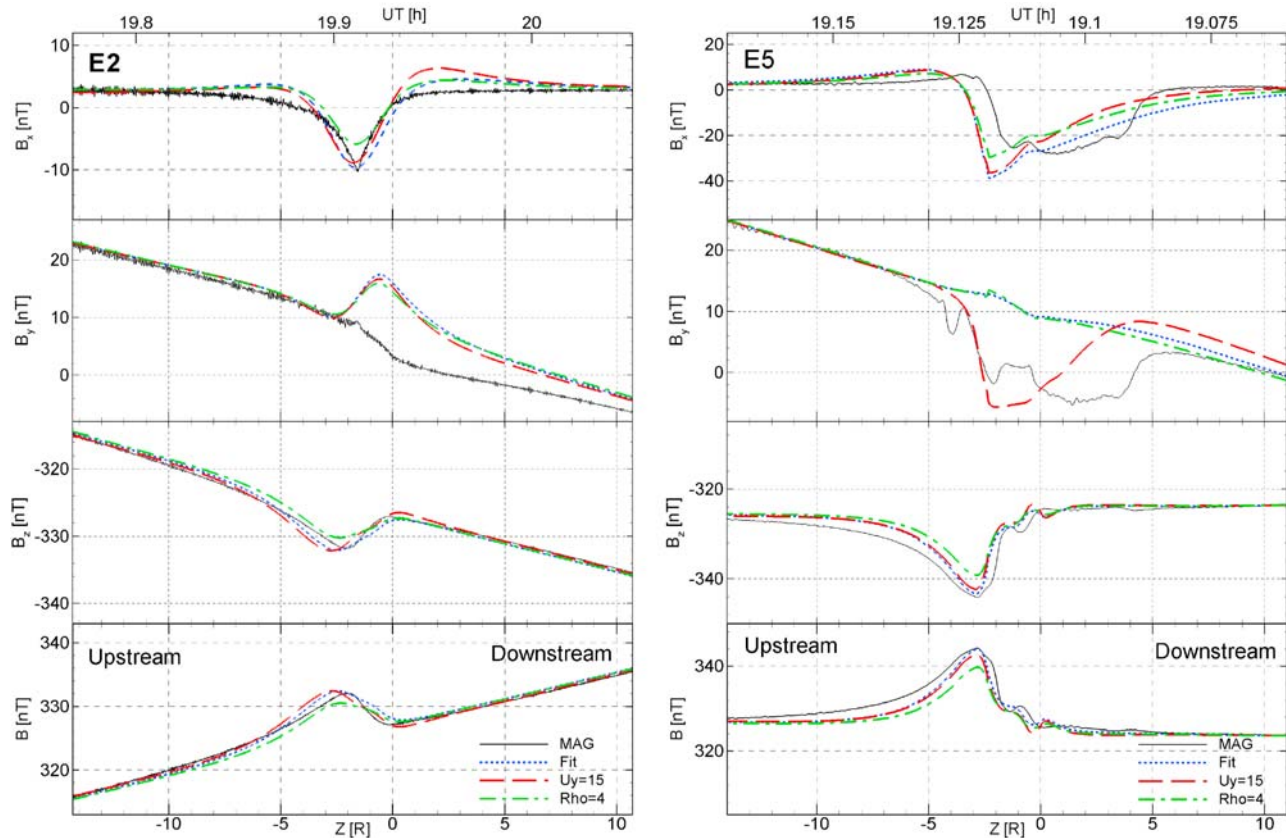
Figure 5. Model-data comparison showing the effect of different upstream conditions: (left) comparisons for the E2 flyby and (right) those for E5. The blue dotted lines denote the same case shown in Figures 2 and 3. Dashed lines (marked "Uy = 15" in the legend) represent a model result with a uniform upstream flow component of $u_y = 15$ km/s. Green dash-dotted lines (marked "Rho = 4" in the legend) represent the result with 33% less upstream ion density.

3 nT and 1 nT stronger perturbations to B_x and B_z, respectively. For the E5 flyby, such a zero tilt angle results in a different shape and a 1 nT and 2 nT weaker intensity in B_x and B, respectively. For the E5 flyby, a 0° tilt angle results in weaker perturbations, in B_x and B_z, because the resulting current system is moved toward upstream. In addition, the locations of the maximum perturbations are also slightly displaced.

[40] Comparing the fits for E2 and E5 flybys, both results are sensitive to the tilt angle of the plume, and an approximate tilt of 10° downstream results in the best fit.

[41] For the E2 flyby, an opening angle of 10° results in 1.5 nT smaller perturbations to both B_x and B, while the shape is similar. For the E5 flyby, an opening angle of 10° results in a 5 nT stronger perturbation to the B_x component. In comparison with the difference made by varying the tilt angle, it is found that the model result is less sensitive to the opening angle than to the tilt angle. In addition, due to the location of individual plumes, gravity and collisions, the opening angle may vary with distance. In this study we find that angles between 10° and 20° are reasonable.

3.6. Case 5: Effect of Upstream Density and Velocity

[42] Cassini observations have found that the electron density in the inner Saturnian magnetosphere varies from 40 cm^{-3} to 90 cm^{-3} [*Gurnett et al.*, 2007]. During the E2

flyby, the Cassini Plasma Spectrometer (CAPS) found significant radial flow from Saturn between -14 to 30 R_E at Enceladus [*Tokar et al.*, 2006]. In this study we compare the effects of such variations in the upstream conditions with two subcases, as shown in Figure 5.

[43] In Figure 5, the magnetometer data and case 2 results are shown by the thin solid lines and dotted lines, respectively. The dotted lines show the subcase result by adding a uniform u_y component of 15 km/s (see case 5-Uy15 in Table 1). This Saturnward velocity component is added to the original upstream velocity that is mainly in the x direction. For the E5 flyby, the uniform u_y decreases the B_x perturbation at the north (downstream) side of Enceladus, while not affecting the B_z component. The fit to B_y is improved, because the u_y component rotates the geometry so that the perturbation to the uniform flow at this location has a large u_y perturbation. When the background u_y is zero, as used in other cases, the E5 trajectory goes through the wake where the flow from both sides of the obstacle meet each other and cancels the flow in the y direction (see Figure 5j, paper 1, the u_y along the x axis). This improvement indicates that such a velocity in the $+y$ direction can be responsible for the unexpected B_y perturbation seen in all flybys.

[44] For the E2 flyby, this u_y decreases the B_x perturbation while not affecting B. However, the B_y perturbation does not

match the observations, suggesting an even larger or non-uniform u_y: The observed B_y perturbation is negative while the simulated B_y is positive around $z = 0$. At this time Cassini is at the coordinate position $(-0.58, 1.81, 0)$ in units of R_E, upstream to the Saturn side of Enceladus. At this location the local mass loading deflects the flow toward Saturn. That is why our interaction model predicts a positive B_y. The observed negative B_y perturbation also requires a localized u_y component away from Saturn. Our test (not shown) indicates that a uniform u_y in the anti-Saturn direction cannot cause such a B_y perturbation, because a uniform flow tends to move the entire flux tube with the flow, rather than bending it. *Saur et al.* [2008] modeled (see their Figure 2) the E2 flyby with multiple jets directing upstream and downstream. Although they did not reproduce enough B_z perturbation, it is found that the downstream plume/jets reproduce the B_y component better than the upstream plume/jets. *Kriegel et al.* [2009] simulated the E2 flyby with a hybrid model, using a plume tilting along the corotation direction and away from Saturn. However, their model cannot fully reproduce the B_y signature either. More detailed study is needed, considering both local interaction and large-scale flow in the Saturn plasma disk, to better decode the information this B_y behavior presents to us.

[45] The dash-dotted lines show case 5-R4 result with an upstream density of 40 cm^{-3}, a 43% decrease from the value used for the best fit case. The result shows a perturbation with similar shape but weaker magnitude. For the E2 flyby both the B_x and B_z perturbations decrease by 30%. For the E5 flyby both the B_x and B_z perturbations decrease by 22%. The percentage difference between the upstream density and the field enhancement indicate that the magnetic field perturbation is dependent but not linearly dependent on the dynamic pressure at the center of mass loading region. At the downstream side, the flow is more diverted in the z direction when passing through the mass loading center, thus the changes in upstream dynamic pressure are less effective on the downstream field than on the upstream field.

[46] The modulation of the perturbations by the upstream density is the result of a charge-exchange-dominant interaction region. In contrast to Enceladus, Titan, Saturn's sixth moon, has a global ionosphere that is dominated by photo ionization processes [e.g., *Simon et al.*, 2008]. The upstream density is found less effective to Titan's perturbation on the ambient magnetic field [*Ma et al.*, 2009].

3.7. Case 6: Comparing the Effect of Photo/Impact Ionization and Charge Exchange

[47] Observations suggest that the charge-exchange process is more important in mass loading the plasma than the photo/impact ionization process around Enceladus [*Pontius and Hill*, 2006]. In paper 1, we have compared the effects of obstacles produced by spherically symmetric photo/impact ionization and charge exchange. It is found that they differ not only in terms of intensity, but also in density and temperature profiles. In this study we quantify the difference between the effect of charge exchange and photo/impact ionization of the plume, and their plasma perturbations along the Cassini trajectory.

[48] As discussed in paper 1, the charge-exchange process differs from the photo and impact ionization processes, because charge exchange does not create a new electron,

and does not modify the net mass flux. In contrast to the more general term "mass loading," the effect of charge exchange is "momentum loading" to the flow. Since photo and impact ionization generate new plasma mass flux, once they reach the velocity of the bulk flow, these new mass can charge exchange with the neutrals. Thus the charge-exchange process that we model in our cases 1–5 includes two types of ions that charge exchange with the neutrals: the torus ions, and the newly added ions by photo/impact ionization. Although we do not track the two types of ions in this study, the total charge exchange and the neutral-torus charge exchange can still both be observed from our results. Two subcases are simulated for each of the E2 and E5 flybys, as shown in Figure 6. For comparison, the plasma density and velocity u_x component are also plotted along the trajectories.

[49] The red dashed lines show the model result with only the charge-exchange process (i.e., without photo/impact ionization processes), as marked "CX" in the legend and Table 1. This subcase shows the effect of charge exchange between the torus ions and plume neutrals. For both flybys, the B_x, B_z and u_x perturbations of case 6 result are 50% less than that of the case 2 result. This indicates that the charge exchange between torus ions and plume neutrals contributes to half the momentum loss of the upstream plasma. The other half should result from the charge exchange between new ions (i.e., from photo/impact ionization processes) and the neutrals. The density profile shows a similar decrease in the wake, while there is no increase in the density increase regions in case 2. This indicates that the density increase caused by the slowdown process (because of momentum exchange with the neutrals) is less effective than the density decrease caused by both deflection and expansion into the wake of the body. The density perturbation in E2 is small for all cases, compared to the E5 result.

[50] The dash-dotted lines are the model result with photo/impact ionization effect only (no charge-exchange effect), as marked by "Ini" in the legends. For both flybys, the result of B_x, B_z and u_x perturbations of case 6 are about 10% that of the case 2 result, indicating that the deceleration of the torus plasma by photo/impact ionization pickup contributes to only a small portion of the total deceleration. The remaining perturbation should come from the total effect of the charge exchange from the two types of ions. The density increase is 50% less than that of the case 2 result. In this nonlinear interaction process, the slowdown of the flow caused by the charge exchange of plume neutrals with both the torus ions and the new ions should be responsible for the rest of the density increase.

[51] As we compare the four plots for each flyby, we see a larger perturbation by the CX subcase than by the Ini subcase, in magnetic field and velocity. However, for the E5 flyby, the density perturbation by the CX subcase is much smaller than that caused by the Ini subcase, between $z = -1.5$ to -5 R$_E$. Cassini is close to the x axis at this time. This difference in the significance of the perturbation can be understood by comparing Figures 3a, 3b, 4a, and 4b of paper 1, in which, along the x axis, the density is increased by the photo/impact ionization case, while slightly decreased by the pure charge-exchange case, due to flow deflection.

[52] In general, these chemical processes are coupled with each other to result in a combined effect of mass flux addition,
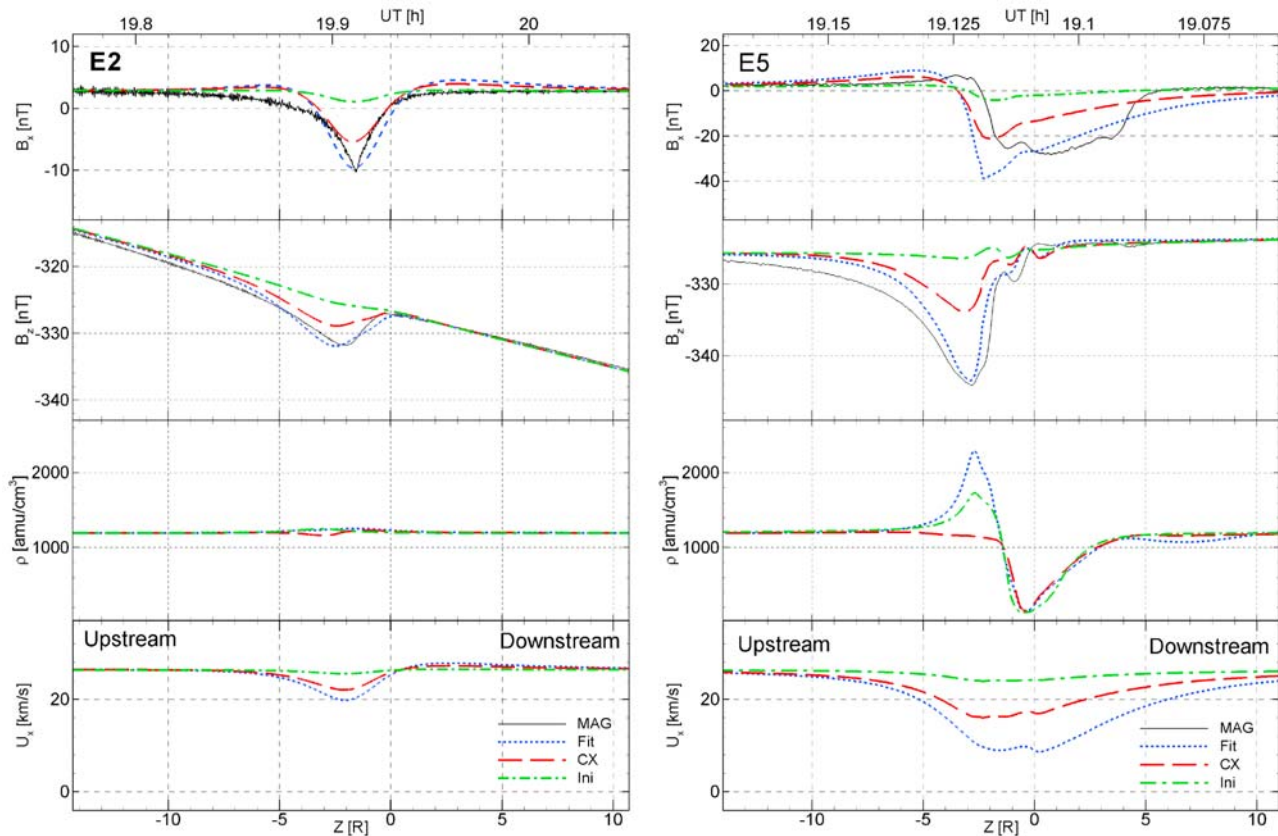
Figure 6. Model-data comparison for the B_x, B_z, density, and u_x component along the Cassini trajectory: (left) E2 results and (right) E5 results. The dotted lines (marked "Fit" in the legends) are best fit results that are used for comparison in Figures 2, 3, 4, and 5. The dashed lines represent results considering charge-exchange effect only (marked with CX). The dash-dotted lines show model results with photo/impact ionization (marked "Ini").

flow deceleration and flow deflection. These changes in the flow add up to bend the magnetic field as observed by the Cassini magnetometer.

4. Summary

[53] Our MHD model, with uniform and homogenous x-directed flow produces satisfactory fits to the B_x and B_z measurements for both upstream and downstream flybys, but the B_y component is not reproduced. It is believed that other effects, such as a noncorotational component of the flow, contribute to such B_y perturbations. Modeling such effects requires moving to a global code that models the circulation of the plasma around Saturn as well as the local interactions. The large radial flows observed by [*Tokar et al.*, 2006] confirm the need for this because these flows are inconsistent with the modeling of the purely local interaction. If we concentrate our attention on the effects associated with the local interaction we can learn much about the plume itself.

[54] A 30% variation in gas production rate causes significant variation in the resultant B_z perturbation. From the case studies shown above, the set of plume configurations during the E2 and E5 flybys suggested by our best fit to the Cassini magnetometer observations using a single plume neutral model are: opening angle of 10° to 20°, and tilt angle

of 10° toward the downstream. Variations in upstream velocity conditions modify the B_x and B_y perturbation, but do not significantly change the B_z perturbation. Variations in upstream plasma density cause less variation in the B_z perturbations compared to the variation in gas production rate.

[55] The photo/impact ionization process results in an approximately 50% ion density increase in the mass loading center against the undisturbed upstream value while the total charge-exchange effect contributes to over 90% of the perturbations to the magnetic field. Among these, the charge exchange between neutrals and the torus ions contributes to about half the momentum loss of the plasma, while the charge exchange between neutrals and newly added ions by photo/impact ionization contributes to the rest.

[56] A strong flow in the y direction is suggested by the case 4 result, and it is likely that this flow is not uniform throughout the Enceladus interaction region. Thus for the next step, it is necessary to model the plasma interaction around Enceladus in a more global context, especially considering the deceleration-resulting imbalance between the centrifugal force and the centripetal force. The incoming flow has a radial force balance between the outward centrifugal force and the inward magnetic stress of the stretched field lines. Post interaction, the slowed flow has less centrifugal force and largely unaltered inward magnetic stress.

Thus the plasma should "fall" in toward Saturn, setting up a global circulation of the plasma around the Enceladus orbit. In addition, detailed studies are still needed to understand the effect of multiple jets in the neutral plume in the region close to the surface of Enceladus.

References

Burger, M. H., E. C. Sittler, R. E. Johnson, H. T. Smith, O. J. Tucker, and V. I. Shematovich (2007), Understanding the escape of water from Enceladus, *J. Geophys. Res.*, *112*, A06219, doi:10.1029/2006JA012086.

Connerney, J. E. P., M. H. Acuna, and N. F. Ness (1981), Saturn's ring current and inner magnetosphere, *Nature*, *292*, 724–726, doi:10.1038/292724a0.

Cravens, T. E., J. U. Kozyra, A. F. Nagy, T. I. Gombosi, and M. Kurtz (1987), Electron impact ionization in the vicinity of comets, *J. Geophys. Res*, *92*, 7341–7353.

Dougherty, M. K., K. K. Khurana, F. M. Neubauer, C. T. Russell, J. Saur, J. S. Leisner, and M. E. Burton (2006), Identification of a dynamic atmosphere at Enceladus with the Cassini magnetometer, *Science*, *311*, 1406–1409, doi:10.1126/science.1120985.

Farrell, W. M., W. S. Kurth, D. A. Gurnett, R. E. Johnson, M. L. Kaiser, J. Wahlund, and J. H. Waite (2009), Electron density dropout near Enceladus in the context of water-vapor and water-ice, *Geophys. Res. Lett.*, *36*, L10203, doi:10.1029/2008GL037108.

Gurnett, D. A., A. M. Persoon, W. S. Kurth, J. B. Groene, T. F. Averkamp, M. K. Dougherty, and D. J. Southwood (2007), The variable rotation period of the inner region of Saturn's plasma disk, *Science*, *316*, 442–445, doi:10.1126/science.1138562.

Hansen, C. J., L. Esposito, A. I. F. Stewart, J. Colwell, A. Hendrix, W. Pryor, D. Shemansky, and R. West (2006), Enceladus' water vapor plume, *Science*, *311*, 1422–1425, doi:10.1126/science.1121254.

Huntress, W. T., Jr. (1977), Laboratory studies of bimolecular reactions of positive ions in interstellar clouds, in comets, and in planetary atmospheres of reducing composition, *Astrophys. J. Suppl. Ser.*, *33*, 495–514, doi:10.1086/190439.

Jia, Y. D., M. R. Combi, K. C. Hansen, T. I. Gombosi, F. J. Crary, and D. T. Young (2008), A 3-D global MHD model for the effect of neutral jets during the Deep Space 1 Comet 19P/Borrelly flyby, *Icarus*, *196*, 249–257, doi:10.1016/j.icarus.2008.03.010.

Jia, Y.-D., C. T. Russell, K. K. Khurana, G. Toth, J. S. Leisner, and T. I. Gombosi (2010a), Interaction of Saturn's magnetosphere and its moons: 1. Interaction between corotating plasma and standard obstacles, *J. Geophys. Res.*, *115*, A04214, doi:10.1029/2009JA014630.

Jia, Y.-D., C. T. Russell, K. K. Khurana, J. S. Leisner, Y. J. Ma, and M. K. Dougherty (2010b), Time-varying magnetospheric environment near Enceladus as seen by the Cassini magnetometer, *Geophys. Res. Lett.*, doi:10.1029/2010GL042948, in press.

Jones, G. H., et al. (2009), Fine jet structure of electrically charged grains in Enceladus' plume, *Geophys. Res. Lett.*, *36*, L16204, doi:10.1029/2009GL038284.

Khurana, K. K., M. K. Dougherty, C. T. Russell, and J. S. Leisner (2007), Mass loading of Saturn's magnetosphere near Enceladus, *J. Geophys. Res.*, *112*, A08203, doi:10.1029/2006JA012110.

Kriegel, H., S. Simon, J. Müller, U. Motschmann, J. Saur, K.-H. Glassmeier, and M. Dougherty (2009), The plasma interaction of Enceladus: 3D hybrid simulations and comparison with Cassini MAG data, *Planet. Space Sci.*, *57*, 2113–2122, doi:10.1016/j.pss.2009.09.025.

Ma, Y. J., et al. (2009), Time-dependent global MHD simulations of Cassini T32 flyby: From magnetosphere to magnetosheath, *J. Geophys. Res.*, *114*, A03204, doi:10.1029/2008JA013676.

Pontius, D. H., and T. W. Hill (2006), Enceladus: A significant plasma source for Saturn's magnetosphere, *J. Geophys. Res.*, *111*, A09214, doi:10.1029/2006JA011674.

Powell, K. G., P. L. Roe, T. J. Linde, T. I. Gombosi, and D. L. De Zeeuw (1999), A solution-adaptive upwind scheme for ideal magnetohydrodynamics, *J. Comput. Phys.*, *154*(2), 284–309, doi:10.1006/jcph.1999.6299.

Saur, J., N. Schilling, F. M. Neubauer, D. F. Strobel, S. Simon, M. K. Dougherty, C. T. Russell, and R. T. Pappalardo (2008), Evidence for temporal variability of Enceladus' gas jets: Modeling of Cassini observations, *Geophys. Res. Lett.*, *35*, L20105, doi:10.1029/2008GL035811.

Simon, S., U. Motschmann, and K. Glassmeier (2008), Influence of non-stationary electromagnetic field conditions on ion pick-up at Titan: 3-D multispecies hybrid simulations, *Ann. Geophys.*, *26*, 599–617.

Spitale, J. N., and C. C. Porco (2007), Association of the jets of Enceladus with the warmest regions on its south-polar fractures, *Nature*, *449*, 695–697, doi:10.1038/nature06217.

Tokar, R. L., et al. (2006), The interaction of the atmosphere of Enceladus with Saturn's plasma, *Science*, *311*, 1409–1412, doi:10.1126/science.1121061.

Tokar, R. L., R. E. Johnson, M. F. Thomsen, R. J. Wilson, D. T. Young, F. J. Crary, A. J. Coates, G. H. Jones, and C. S. Paty (2009), Cassini detection of Enceladus' cold water-group plume ionosphere, *Geophys. Res. Lett.*, *36*, L13203, doi:10.1029/2009GL038923.

Tóth, G., et al. (2005), Space Weather Modeling Framework: A new tool for the space science community, *J. Geophys. Res.*, *110*, A12226, doi:10.1029/2005JA011126.

Waite, J. H., et al. (2006), Cassini Ion and Neutral Mass Spectrometer: Enceladus plume composition and structure, *Science*, *311*, 1419–1422, doi:10.1126/science.1121290.

T. I. Gombosi and D. Najib, Department of Atmospheric, Oceanic and Space Sciences, University of Michigan, Ann Arbor, MI 48109, USA.

Y.-D. Jia, K. K. Khurana, Y. J. Ma, and C. T. Russell, IGPP, University of California, Los Angeles, CA 90095, USA. (yingdong@ucla.edu)